A self-assembled flavin protective coating enhances the oxidative thermal stability of multi-walled carbon nanotubes

CrossMark

Somin Kim [a], Myungsu Jang [a], Minsuk Park [a], No-Hyung Park [b], Sang-Yong Ju [a, *]

[a] Department of Chemistry, Yonsei University, 50 Yonsei-ro, Seodaemun-Gu, Seoul 03722, South Korea
[b] Department of Textile Convergence of Biotechnology and Nanotechnology, Korea Institute of Industrial Technology, 1271-18 Sa 3-dong, Sangnok-gu, Ansan-Si, Gyeonggi-Do 426-910, South Korea

ABSTRACT

Multi-walled carbon nanotube (MWNT) has many commercial applications. However, its broad use is limited by the surface-bound oxygen lowering its thermal stability. Here, we developed a facile method to enhance the oxidative thermal resistance of MWNTs that involves molecular coating promoted surface passivation. In the approach, ball milling is employed to self assemble flavin mononucleotide (FMN) helically around MWNTs through non-covalent interactions with no increased defects in MWNT. Upon high temperature oxidation, the ribityl phosphate side chain of FMN in the nanoconstruct undergoes partial decomposition to generate a corresponding isoalloxazine derivative on the surface of the MWNTs. Transmission electron microscopy reveals that the oxidatively annealed material is comprised of a tight isoalloxazine coating stacked on the sidewalls of the MWNT. The results of thermal gravimetric analysis studies show that the coating further elevates long-term stability and the energy barrier for oxidation of the MWNT by 28 kJ/mol from 113 kJ/mol for the bare MWNT. The role of the isoalloxazine coating is proposed to be surface passivation from molecular oxygen. As a consequence of the passivation, the maximum oxidative temperature of the MWNT is raised to 938 K as compared to that of 843 K for bare MWNT.

© 2017 Elsevier Ltd. All rights reserved.

1. Introduction

Multi-walled carbon nanotubes (MWNTs), concentric cylindrical rolls of graphene sheets, have excellent electrical and thermal properties [1,2]. As compared to single-walled carbon nanotubes (SWNTs), MWNTs are amenable to economical (<$100 per kg) [3] large scale production. As a result, several applications exist for these materials including light-weighted battery electrodes [4,5], electromagnetic interference shielding [6], and high-performance polymer composites [7—9] and flame retardant additives [10] and hinge on high thermal stabilities in an air atmosphere.

Thermal stabilities of MWNTs, often given in terms of oxidation temperatures, are a direct consequence of the presence of aromatic rings within their structures. As a result, the thermal stabilities of these materials are influenced by the number and diameter of the walls [11,12], the length of the tube [13], and the presence of residual catalysts and/or defects. As compared to graphene, which is

stable up to 873 K [14—16], MWNT have inferior thermal stabilities in an air atmosphere owing to strain caused by the curvature of the π conjugated networks [11]. Generally, the maximum oxidation temperatures (T_p) of MWNTs, obtained using thermogravimetric analysis (TGA), varies from material-to-material in a range of 673—773 K [11,17,18]. It is known that oxidative degradation pathway of MWNTs involves reversible adsorption of gaseous O_2 on the basal graphene sidewalls to form mobile/static oxygenated carbons or direct reaction with edge carbon atoms leading to rapid CO_2 formation [19,20].

A facile approach to improve the oxidation stabilities of MWNTs is a necessary component of efforts to broaden applications of these materials. Our recent studies aimed at this goal focused on the use of flavin mononucleotide (FMN) as a carbon nanomaterial stabilizing agent. This substance (Fig. 1A), a phosphate monoester of riboflavin (RF) that serves as a redox cofactor in many enzymatic transformations [21], is known to disperse various nanomaterials as effective and selective manner [22—31]. In those study, it was shown that FMN wraps around SWNTs in a tight helical manner (Fig. 1C) as a consequence of π-π interactions between isoalloxazine rings of FMN and the graphene sidewalls. In addition,

---

* Corresponding author.
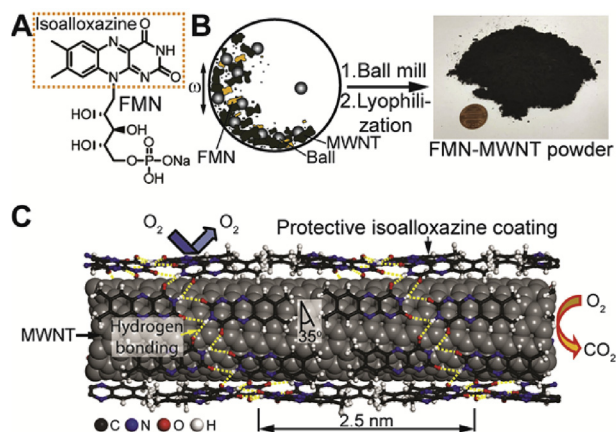 *E-mail address:* syju@yonsei.ac.kr (S.-Y. Ju).

Fig. 1. Schematic of ball mill assisted FMN coating of MWNT. (A) Structure of FMN. (B) Ball mill assisted formation of non-covalent functionalized MWNT with FMN. Photograph: large scale preparation of FMN-MWNT powder. (C) Schematic representation of the enhanced thermal stability of MWNT helically wrapped by the isoalloxazine passivation layer, which prevents MWNT oxidation. The FMN tail is omitted for visual clarity. (A colour version of this figure can be viewed online.)

quadruple intermolecular hydrogen-bonding (yellow dotted line) exists in this complex between uracil components of the FMN structure. The tight FMN helix might protect the MWNT surface by protecting oxygen binding.

In the investigation described below, we found for the first time that the oxidative thermal stability of MWNTs is enhanced by surface protection of small molecular organic flavin mononucleotide (FMN) wrapping. Vibrational ball mill method in the presence of FMN produces non-covalent, individualized, and shortened MWNT functionalization in effective and scalable manner. Atomic force microscopy (AFM) reveals that the organic coating consists of a tight helical self-assembly of FMN which is stacked on the MWNT sidewalls via π-π interaction. Especially, TGA along with liquid chromatography (LC)-mass spectroscopy (MS) show that, upon high temperature oxidation, the ribityl phosphate tail group of FMN partially decomposes, leaving the isoalloxazine sheath on MWNT surface. Such sheath passivates MWNT surface from oxidation by elevating oxidation activation energy (E_a) barrier by 28 kJ/mol, calculated by heating rate programmed TGA measurements. High resolution transmission electron microscopy (HRTEM) shows that the isoalloxazine on the MWNT remains intact as a coating. As a result, FMN-wrapped MWNT by π-π interaction displays enhanced thermal stability up to 933 K, departed from that (843 K) from MWNT only.

2. Experimental

2.1. Methods and materials

MWNT (diameter: ca. 11 nm, length: <40 μm, wall number: 10—11 layer) was kindly donated by LG Chemicals. FMN sodium salt (purity >93%) was purchased from TCI. Deionized (DI) water whose electrical resistance is greater than 18 MΩ was used throughout the experiment. HPLC-grade solvents are utilized for LC-MS measurements. Atomistic molecular structure of FMN-MWNT was generated and visualized by using Materials Studio according to the literature reported elsewhere [23]. Prior to scanning electron microscope (SEM) and Raman measurements, 285 nm thick SiO2/Si substrates were piranha-cleaned, followed by washing with DI water, and final N2 drying. SEM images were acquired by using a JSM-7001F (JEOL Ltd.) with a 15 kV acceleration. Length

distributions were obtained by analyzing 100 MWNTs. Raman spectra were acquired by using a custom-made setup [25,32] with 532 nm laser with 1 mW via a backscattering geometry. The Si peak (520.89 cm^{-1}) was used as an internal reference. UV—vis—NIR absorption spectra were obtained by using JASCO 770 with a cuvette having 10 mm beam path. For absorption measurements, 7.0 mL DI water was added to 0.1 g of the milled MWNT sample, and the supernatants were collected by decantation after settlement of large MWNT bundles. LC-MS spectra were acquired by using 3100 an LC-MS instrument (Waters). FMN and FMN-MWNT samples, following annealing at 543 and 723 K, respectively, under air for 1 h in a conventional quartz tubular reactor [32], were dissolved in N,N-dimethyl formamide (DMF). The mixtures were filtered using a 0.45 μm pore poly(tetrafluoroethylene) (PTFE) syringe to remove MWNT. After addition 0.1% trifluoroacetic acid, the solutions were subjected to LC using an acetonitrile and DMF gradient and a C18 reverse phase column. Electrospray ionization (ESI) MS spectra were acquired in a positive mode.

2.2. Non-covalent functionalization of MWNT with FMN

Vibrational ball milling was performed by using Pulverisette 23 (Fritsch, German) operated at ω = 50 Hz to functionalize MWNT with FMN. Briefly, a mixture of 0.10 g of MWNT and 0.08 g of FMN in 3.0 mL water was introduced into the milling setup with 2 %-v of zirconia balls (diameter = 5 mm). The milled samples were collected at time intervals of 5, 10, 30, 60, and 90 min. The samples were vacuum-filtered by using a Buchner funnel with a water-circulated aspirator (Eyela A-3S). The black MWNT paper was washed with water several times to remove free FMN. The sample was subject to lyophilization for 2 d to produce dry FMN-MWNT powder.

2.3. AFM measurements

AFM images were acquired by using the tapping mode with a Nanowizard I (JPK Instrument). Dried FMN-MWNT was dispersed in DI water, and 20 μL aliquot of the dispersion was dropcast onto freshly-cleaved mica substrate. Height and phase topographies were obtained by using an Al-coated silicon cantilever (force constant: 37 N/m, ACTA-20, App Nano) resonated at 361.96 kHz. The acquired 512 × 512 pixel images were flattened by using a polynomial routine.

2.4. TGA-differential scanning calorimetry (DSC) measurements

Thermal properties of the samples were obtained mainly by using a simultaneous TGA-DSC analyzer (STA80000, Perkin Elmer). For this purpose, ca. 10 mg of dried FMN-MWNT samples along with bare FMN and MWNT were loaded onto alumina pans. Bare FMN was initially annealed at 373 K for 1 h to eliminate adsorbed water. A typical scanning range was from 293 K to 1173 K with a ramping rate (β) of 5 K/min with a 100 standard cubic centimeter per min (sccm) flow of synthetic air composed of 21 v.% O2 in N2 unless otherwise noted. E_a measurements of MWNT derivatives were conducted using a narrower range (i.e., 573—1023 K) by varying β (i.e., 2, 5, 10, 20 K/min).

2.5. HRTEM and electron dispersive X-ray spectrometry (EDS) measurements

These measurements were made by using a spherical aberration-corrected scanning TEM (JEOL JEM-ARM 200F) with a 200 kV acceleration voltage. The 723 K annealed FMN-MWNT sample in water was briefly sonicated for 30 s, and the resulting

dispersion was dropcast on a copper TEM grid covered with an ultra-thin carbon support (LC200-Cu, Lot#: 110727, 200 mesh, Ted Pella). After 3 min of incubation, excess material was removed by washing with water. EDS line spectra were acquired by using an 80 mm^2 SDD detector (X-MaxN 80 T, Oxford instruments).

2.6. Electrical measurements

The sheet resistances from bare MWNT and 60 min milled FMN-MWNT film were measured by four point probe (RS55/tc, KLA-Tencor). Film samples were prepared by the filtration of the briefly-sonicated dispersion. The filtered MWNT mats were further dried at 383 K under ~3 mTorr vacuum. Both samples were subject to sheet resistance measurements before and after 753 K air-annealing for 1 h. The film thicknesses from the MWNT and FMN-MWNT was measured by DektakXT Stylus Profiler (Bruker) to be ~10 and 15 μm.

3. Results and discussion

Non-covalent functionalization of MWNT with FMN is achieved by using the vibrational ball mill schematic shown in the left of Fig. 1B. MWNT and FMN (10:8 weight (wt) ratio, total 6.0 wt % in deionized water) are added to a ball miller containing zirconium milling balls (see Experimental for details). Ball milling, operating by impact and attrition of the balls during rotation or vibration of the container [33,34], results in the formation of a viscose homogeneous black syrup, which upon lyophilization produces a fluffy black powder (see the photograph in Fig. 1B).

The results of an atomic force microscopy (AFM) study reveals the details information on how the noncovalent surface functionalization of MWNT by FMN occurs. The sample for this measurement was prepared by dispersing FMN-MWNT in water followed by brief 1 min sonication and drop casting on mica substrate. In Fig. 2 is shown representative phase and height images of FMN-functionalized MWNTs (see Fig. S1A and B in the Supporting Information (SI) for the corresponding height images). The measured heights of MWNT are in the 9.6–11.7 nm range (Fig. 2A, Fig. S1A and

S1B), which is in agreement with the quoted median diameter (i.e., 11 nm) of the MWNT. The phase image, which in comparison to the height image is sensitive to chemical composition, adhesion and friction [35], enables ready identification of FMN organization on the MWNT. As compared to the straight and clean surface of as-received MWNT (see TEM images in Fig. S2A and B of SI), the surface of FMN-coated MWNT displays helical wrapping. Inspection of the enlarged height image (Fig. 2B, Fig. S1A and S1B) reveals that a large number of lumps indicative of FMN deposits exists along the nanotube axis, even though multiple washing steps were performed. The period of peak to peak striation is ca. 95 nm and the height difference from peak to trough is 2 nm, which originates from collapsed adjacent d-ribityl phosphate moieties of FMN [23]. The discrepancy between the observed striation periodicity and the predicted value of 2.5 nm (Fig. 1C) likely originates from the large curvature of the AFM tip (typically >10 nm). This observation suggests that FMN strongly binds to the MWNT surface. In addition, FMN in FMN-MWNT is self-assembled on the surface in right- (Fig. 2B and Fig. S1B) and left-handed (Fig. S1A and B) helical configurations. The helices extend to the ends without undergoing changes in their helical handedness. The helical pitch was found to vary from 25 to 41° with respect to the diameter direction. This pitch is in line with the 35° pitch from an atomistic 8_1 FMN helix (Fig. 1C) and is related to hydrogen bonding interactions of self-associating FMN [22,23,25] and the pitch variation seems to be associated with an underlying MWNT chirality [36]. The results of the AFM studies provide strong evidence that a tight helical wrapping of MWNT by FMN exists in FMN-MWNT as a consequence of strong π-π interactions.

The length variations of FMN-MWNT prepared using different milling times were determined by analyzing SEM images (Fig. 3A and Fig. S3A-E). Inspection of representative SEM images of samples derived from 60 min milling (Fig. 3A) shows that, in agreement with the AFM results, the MWNTs are highly individualized with few μm lengths. The length histograms of each sample (Fig. 3B) are best fitted with a log normal distribution. Overall, the lengths of the MWNTs decrease as the milling time increases (inset of Fig. 3B). Specifically, the average lengths of samples produced using 5 and 90 min milling are 2.0 and 1.2 μm, respectively.

The possible occurrence of defects in MWNT wrapped by FMN arising during milling was assessed by utilizing micro Raman spectroscopy (see Experimental for details). In Fig. 4 are displayed normalized Raman spectra of FMN-MWNT samples prepared using different mill times, along with that of as-received MWNTs. The spectra contain three prominent peaks at ca. 1348, 1587 and 2688 cm^{-1} which corresponds to D (disorder), G (graphitic) and 2D (overtone of D) bands, respectively. This intensity pattern is reminiscent of those seen in typical MWNTs [37]. The plot of D to G band intensity ratio (I_D/I_G, Fig. S4), which can be utilized to parameterize
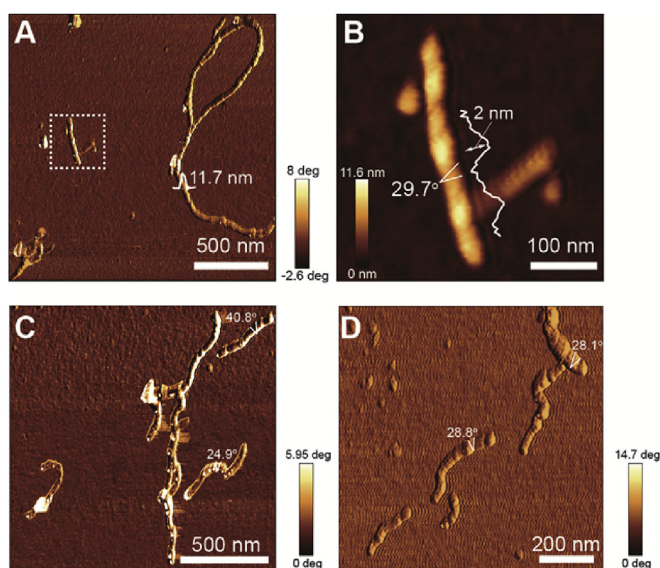

Fig. 2. Characterization of helically coated FMN on MWNTs. AFM (A) phase and (B) the enlarged height images of dotted box in A, showing helical FMN assembly on MWNTs. (C and D) Variation of helical pitch of FMN assembly on MWNT. (A colour version of this figure can be viewed online.)
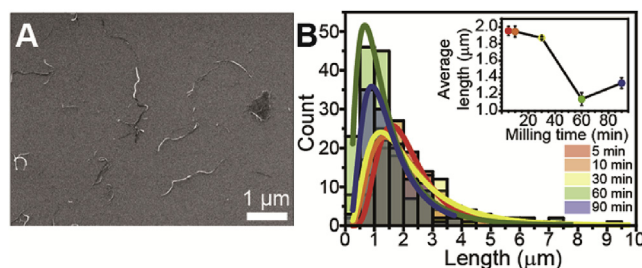

Fig. 3. (A) Representative SEM image of FMN-MWNTs prepared by 60 min milling. (B) Log-normal length histograms of FMN-MWNT as a function of milling times. Inset: average length trends of MWNTs as a function of milling times. (A colour version of this figure can be viewed online.)
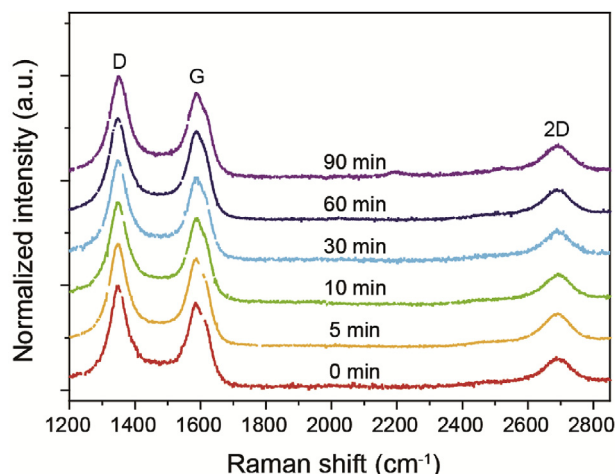
Fig. 4. Raman spectra of FMN-MWNT samples as a function of milling times along with that of as-received MWNT. (A colour version of this figure can be viewed online.)

nanotube defects [38], of as-received MWNT is about 1.2 and this ratio is maintained throughout milling. Along with the observed length histogram, this finding strongly suggests that ball milling effectively shortens the MWNT length without introducing noticeable defects.

The absorption spectra of FMN-MWNT samples (Fig. S5) were determined on the supernatants obtained by addition of the powder to water followed by decantation (see Experimental). The absorption spectra are sloped upward to high energy region owing to the existence of a nanotube plasmon peak (ca. 260 nm) originating from the M point of the Brillouin zone [1]. Analysis of the spectra shows that the sample obtained by using 60 min milling has the highest MWNT dispersion. As a result, a 60 min milling time was used to prepare samples employed in remainder of this study unless otherwise noted.

The most important observation made in this investigation is that MWNT noncovalent functionalized with FMN has a high stability toward thermal oxidation. In Fig. 5A are displayed TGAs of FMN, MWNT and the ball-mill generated FMN-MWNT along with the corresponding differential curves (see Experimental for their measurement details). These profiles show first that as-received MWNT has an onset decomposition temperature of 723 K and a T_p (the peak of the differential curve in the bottom) of 846 K. The corresponding DSC curve (red trace of Fig. S6) shows similar thermal pattern with the differential curve and confirms that majority of thermally induced weight change originates from exothermic decomposition of MWNT. The ca. 8 %-wt that remains after 923 K treatment is associated with the catalyst used for MWNT formation.

Before describing the TGA of FMN, it is informative to know the

thermal behavior of the related flavin, RF. Mastowska and coworker [39] described the thermal degradation of RF based on analysis of TGA and DSC data. Specifically, these workers showed that thermal degradation of RF is initiated by loss of three molecules of water (13% by wt loss) from its *d*-ribityl side chain at 553 K, followed by degradation at 573 K (21wt-% loss) to give a pyrrole, and then formation and degradation of lumichrome (tautomerized form of isoalloxazine) at 623 K. Similarly, we observed that FMN displays three major thermally induced weight losses at 543, 648 and 713 K. The corresponding major DSC peaks (black curve of Fig. S6) displays exothermic heat flows. The initial slow endothermic weight loss up to ~543 K (10.4 %-wt) in Fig. S6 is associated with departure of three water molecules in the *d*-ribityl phosphate group of FMN resulting from dehydroxylation, leading to unsaturated carbon chain (Fig. 5B). The second and third weight losses occurring at 648 and 713 K (22.6 and 17.0%-wt) are likely associated with removal of phosphate group and a two carbon units from the FMN side chain. The weight differences between suggested and calculated structure (Table S1) are nearly identical within 3%, which supports the proposal that the decomposition product is the one shown in Fig. 5B. The formation of this *N*-propenyl-isoalloxazine derivative upon 543 K annealing of FMN (see Experimental and Fig. S7A and B) was confirmed by using LC-MS spectroscopy. The mass spectrum of the major peak in the chromatogram with a retention time of 10.6 min has $m/z = 282.26$ ([M + H]$^+$). This value corresponds to the mass of the unsaturated isoalloxazine derivative shown in the right part of Fig. 5B.

The thermogram of FMN-MWNT (blue curve in Fig. 5A) shows three weight losses occurring at 541, 718 and 938 K. Because MWNT itself does not display decomposition peaks below 723 K, the weight losses observed at 541 and 718 K likely originate from the FMN moiety. Surprisingly, the major T_p of FMN-MWNT observed at 938 K is greater by ca. 90 K than that (846 K) of bare MWNT. In order to understand the origin of the enhanced thermal stability of FMN-MWNT, LC-MS spectra of the 723 K annealed were acquired. Analysis of the LC-MS data (Fig. S8A and B) shows that the major product is similar to the isoalloxazine derivative generated by 543 K annealing of FMN. The major peak in the chromatogram has a retention time of 10.69 min and a $m/z = 309.18$ ([M + H]$^+$), which corresponds to the *N*-pentadienyl- isoalloxazine derivative shown in the inset of Fig. S8B and similar structure as shown in Fig. 5B. Although the exact origin for the formation of the differently oxidized products from FMN only and FMN-MWNT (*i.e.*, propenyl vs pentadienyl sidechains, respectively) is unknown, it is suggested that the local environment near MWNT might provide less alkyl-decomposing atmosphere due to van der Waals interaction between alkyl sidechain and MWNT.

More strong evidence that FMN-wrapped MWNT exhibits superior thermal properties is obtained from thermal behavior of FMN-MWNT and MWNT both pre-annealed at 723 K for 1 h. Fig. 6A
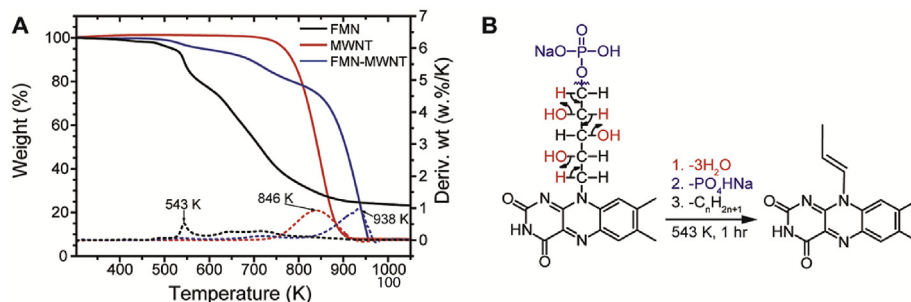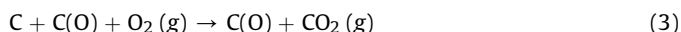

Fig. 5. (A) TGAs of FMN, MWNT, and FMN-MWNT samples with a heating rate of 5 K/min under an air atmosphere. The dotted lines correspond to differential curves. (B) The suggested FMN decomposition process via dehydration. (A colour version of this figure can be viewed online.)

displays the thermograms of FMN-MWNT (red) and MWNT (black). Although the 1 h annealing step lowers T_p of both samples by ~40 K as compared to those in Fig. 5A, T_p difference between two samples remains similar (*i.e.*, 97 K), in good agreement with the case of FMN-MWNT and MWNT without the annealing step. We also conducted isothermal measurement of both annealed samples at 723 K for prolonged period of time, as shown in Fig. 6B. Notably, the isothermal treatment starts to differentiate weight losses immediately and, after the 3 h treatment, the weight of the FMN-MWNT drops by only 8% as compared to 77% in the case of MWNT. This result undoubtedly demonstrates the passivative role of the remaining isoalloxazine on MWNT against O_2.

This result indicates that, despite the high annealing temperature employed, the isoalloxazine ring in FMN-MWNT remains intact. It should be pointed out that the peak shapes of the derivative curves (dotted line in Fig. 5A) arising from bare MWNT and FMN-MWNT are different. Specifically, the peak shape of bare MWNT is close to symmetric while that of FMN-MWNT is asymmetric with a tail toward the low temperature end. This finding indicates that FMN-MWNT reacts with O_2 at the later stage presumably because of passivation offered by the isoalloxazine moiety. The rationale of this observation suggests that the direct reaction of O_2 with the tube ends to produce CO_2 might be facilitated at the later stage of the thermogram. As a result, the observed peak asymmetry suggests that shorter MWNT would exhibit lower thermal stability because the high density of MWNT ends would accelerates MWNT end oxidation.

In fact, the experimental results show that T_p of FMN-MWNT decreases as the length of its chain is shortened. In Fig. 7A are displayed TGA thermograms of FMN-MWNT produced by using different milling times. With increasing milling time (Fig. 7B) and subsequent shortening, the produced FMN-MWNT was found to have a lower T_p from the asymmetric peak of the derivative curve. For instance, the observed T_p of FMN-MWNT derived using 5–90 min milling times changes from 926 to 897 K (a 29 K difference). Because MWNT defects do not increases during milling as seen in Raman study, these observations show that a decreased MWNT length results in a decrease in thermal stability as shown in inset of Fig. 7B, a conclusion that is in agreement with literature reports [40].

Those results direct us to consider oxygen-related decomposition mechanism of MWNT. When carbon nanotube (or graphene) reacts with molecular oxygen, there is a general agreement about the following steps (Eqs. (1)–(4)) [19,20].

$$2C + O_2 \rightarrow 2C(O) \tag{1}$$

$$C(O) \rightarrow CO\ (g) \tag{2}$$

$$C + C(O) + O_2\ (g) \rightarrow C(O) + CO_2\ (g) \tag{3}$$

$$2C(O) \rightarrow C + CO_2\ (g) \tag{4}$$

where C(O) stands for static and mobile oxygen surface species. A detailed and comprehensive mechanism of graphene combustion is based on theory and a literature by Radovic [19]. According to this model both direct and indirect routes to CO_2 evolution exist. Gas phase O_2 can either adsorb reversibly on the MWNT sidewalls to form mobile epoxide-type oxygen (Eq. (1)) or react directly with carbon edge atoms. The oxygen-saturated MWNT edge is then highly susceptible to the mobile species resulting in rapid CO_2 formation (Eqs. (3) and (4)), along with CO formation (Eq. (2)) to lesser extent. This indicates a complex multistep surface reaction rather than a direct attack of O_2 at the carbon atom to be gasified. Therefore the passivation of the MWNT surface results in less probable formation of C(O) and ultimate CO_2 at the end of MWNT, and the increased population of MWNT ends by length shortening is expected to have lower thermal stability.

In order to gain more information about the existence of the isoalloxazine derivative on the MWNT surface, the 723 K annealed FMN-MWNT sample was subjected to AFM and HRTEM analysis. First, as shown in Fig. S9, AFM height (A and C) and corresponding phase (B and D) images of the annealed FMN-MWNT does not display profound deposits of FMN anymore and shows rather smooth height and phase profile along the tubes. Upon closer inspection, one can still observe that MWNT maintains the striation with slightly shorter periodicity (75 nm, Fig. S9C) mentioned in the earlier AFM results (*i.e.*, 95 nm). This result supports that the smooth surface probably originates from the shorter chain length of pentadienyl sidechain than that of ribityl phosphate of FMN. Although it has quite uniform surface, it is difficult to discern whether those features originate from partially-decomposed FMN derivative(s). For this, we further resort to HRTEM measurement. In Fig. 8A and B are shown the HRTEM images of this sample at different magnifications (see Fig. S10 for an additional low magnification TEM image). The image shows that the MWNTs in the annealed FMN-MWNT exist as highly entangled structures with occasional open ends. Inspection of the higher magnification image (Fig. 8B) reveals that the sidewalls of MWNT in 723 K annealed FMN-MWNT have an interlayer spacing of 0.37 nm and contain an absorbed organic residue (red arrow). While the crystallinity of MWNT still exists, in contrast to the clean surface of as-received MWNT (Fig. S2) the annealed sample contains a physisorbed organic residues. Finally, analysis of the Raman spectra of the annealed sample (Fig. S11) shows that the I_D/I_G ratio (i.e., 1.21) remains close to that of the un-annealed FMN-MWNT (i.e., 1.2), suggesting that if any defects are introduced during annealing, it is negligible.
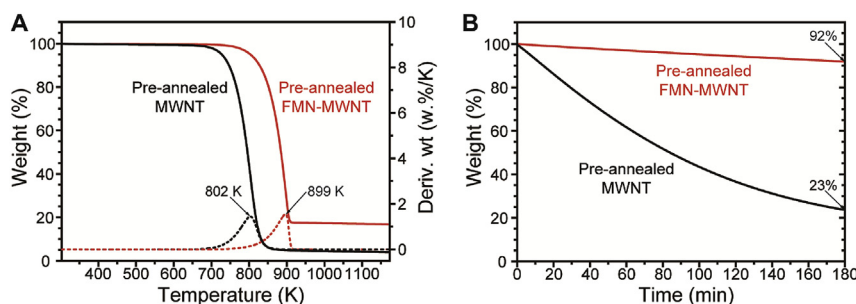

Fig. 6. (A) TGAs of pre-annealed FMN-MWNT (red) and MWNT (black) samples at 723 K for 1 h. The dotted lines correspond to differential curves. (B) The isothermal TGAs of both samples at 723 K. (A colour version of this figure can be viewed online.)
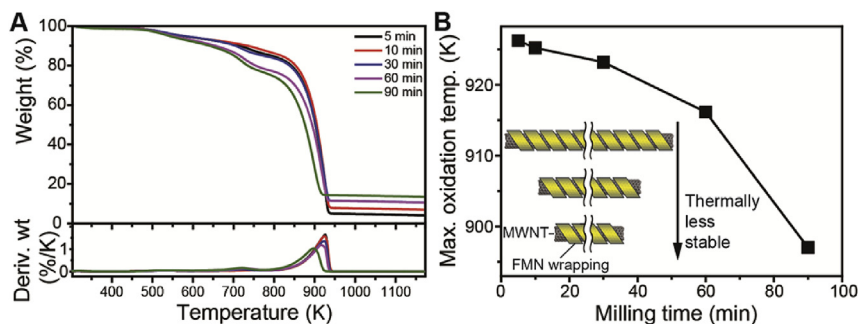
Fig. 7. (A) Variation of the maximum oxidation temperature of FMN-MWNTs with increasing milling time. (B) Length effect of FMN-MWNT on T_p. (A colour version of this figure can be viewed online.)

In order to probe the existence of an isoalloxazine derivative observed in the AFM study, the EDS line spectrum along the interface between MWNT and the organic residue in annealed FMN-MWNT indicated by red line in Fig. 8C was analyzed in terms of its carbon, nitrogen and phosphorus profiles (Fig. 8E). The results show that the carbon content is larger on the MWNT sides and lesser on physisorbed organic sides of the interface. This observation is in good agreement with the cross sectional schematics of MWNTs (Fig. 8D), which show that carbon compositions are higher on the MWNT side. The phosphorus cross section in the EDS line spectrum (top) shows that functionalities containing phosphorus are separated by ca. 2 nm. On the basis of phosphate distance (ca. 6 Å) in adjacent FMNs on MWNT (Fig. 8F), the result suggests that at least one third of the phosphate groups of FMN are removed during 723 K annealing. Most strikingly, the cross sectional nitrogen composition (middle panel of Fig. 8E) has quasi-periodic placement with a 0.3—0.5 nm periodicity. This distance is similar to the intermolecular distance between the nitrogen atoms of helically organized isoalloxazine on the MWNT surface (Fig. 8F) and different from the smaller 0.2 nm periodicity associated with intramolecular nitrogen distance. The combined observations provide further evidence in support of the conclusion drawn from the results of TGA and LC-MS studies that FMN undergoes only partial decomposition during annealing. Thus, the isoalloxazine derivative formed by partial decomposition of FMN remains intact on the MWNT sidewalls during the annealing step and serves as the main contributor to the enhanced thermal stability of the FMN-functionalized MWNTs.

An important question arising from this conclusion is how the isoalloxazine derivative enhances the oxidative stability of MWNT. We found that the effect originates from elevation of E_a of MWNTs by the presence of an isoalloxazine coating. To arrive at this conclusion, the E_a of oxidative FMN-MWNT decomposition was calculated by utilizing heating rate (β)-programmed TGA analysis with Kissinger's model based on the following Arrhenius-type formal rate law (Eq. (5)) [17,41]. The temperature at which the maximum mass loss occurs for different βs is expressed by:

$$\ln \frac{\beta}{T_p^2} = -\frac{E_a}{RT_p} + \ln \left[\frac{df(\alpha)}{d\alpha} \right] \frac{AR}{E_a} \tag{5}$$

where $f(\alpha)$ is the conversion function, A the pre-exponential factor and R the ideal gas constant (8.31 J/mol·K).

To generate E_a, TGA traces of as-received MWNT (Fig. S12A) and 723 K annealed FMN-MWNT (Fig. S12B) were generated at different β values (*i.e.*, 2, 5, 10, and 20 K/min) and the resulting derivative curves (Fig. S12C and D) were constructed. Analysis of plots of $\ln(\beta/T_p^2)$ vs. $1/T_p$ shows that T_p increases as β Increases. In addition, the shape of derivative curve for bare MWNT displays a symmetric to asymmetric peak transition with increasing β, whereas that from annealed FMN-MWNT exhibits persistent asymmetry. This finding suggests that, as they do with MWNT high β values facilitate end group oxidative decomposition of FMN-MWNT. The E_a of MWNT and FMN-MWNT, obtained by using linear regression treatment (Fig. 9A), are 113 and 141 kJ/mol, respectively. This difference (28 kJ/mol) is much larger than that of MWNT enhanced by addition of P_2O_5 (19 kJ/mol) [20], demonstrating that the improved thermal behavior of FMN functionalized MWNTs stems from an enhancement of E_a for oxidative decomposition caused by the presence of the isoalloxazine shell (Fig. 9B). The large calculated binding energy (ca. 2 eV) between isoalloxazine and a carbon nanotube [42] is consistent with the observed E_a elevation of ca. 0.29 eV.

We further demonstrate the role of FMN passivation on MWNT sheet resistance upon annealing. As shown in Fig. 10, the sheet resistance of the FMN-MWNT and bare MWNT films before the annealing at 753 K for 1 h are 13.2 and 9.1 Ω/sq (see Experimental for the details). We observed that annealing above 753 K results in the shrinkage in the bare MWNT film by ~50%, followed by becoming ashes. After 1 h air-annealing at 753 K under air
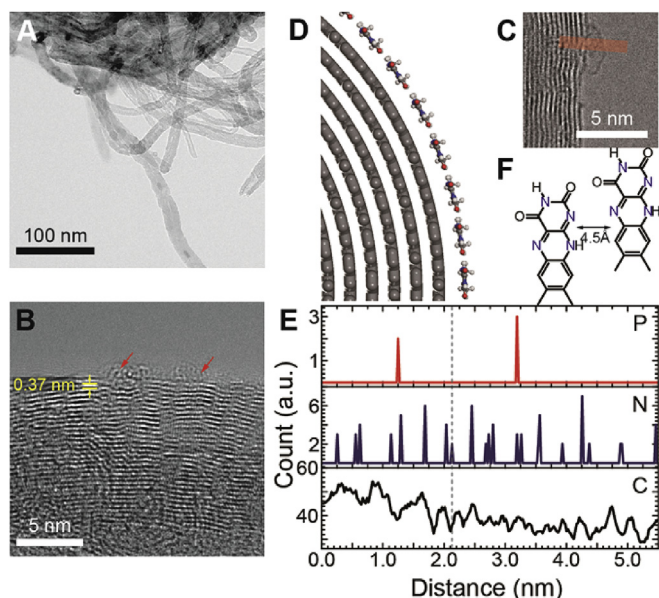

Fig. 8. HRTEM images of (A) agglomerated FMN-MWNTs and (B) a physisorbed organic material on MWNT sidewall after 723 K annealing. (C) EDS line scan position (red) at the interface between physisorbed organic material and MWNT. (D) Schematics of isoalloxazine dimer on MWNT. (E) Atomic contents according to C, N, and P along the distance. (F) Intermolecular distance between adjacent FMNs. (A colour version of this figure can be viewed online.)
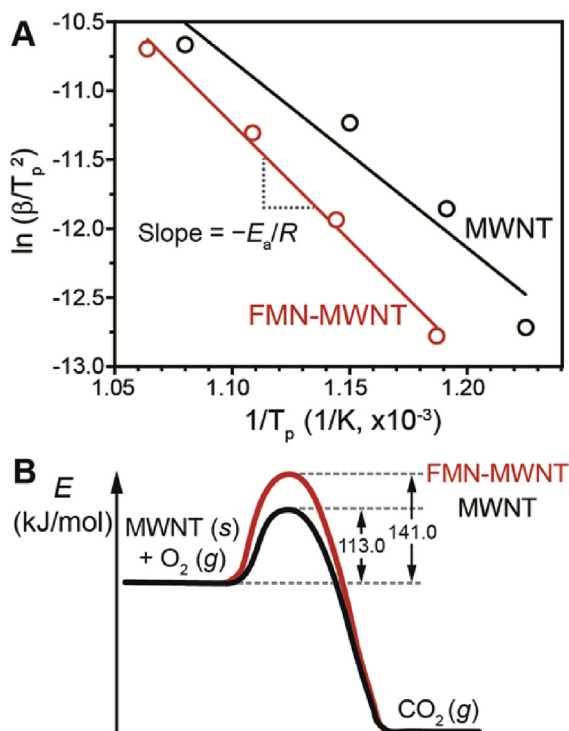
Fig. 9. The E_a of MWNT and FMN-MWNT oxidation. (A) Plot of ln (β/T_p^2) as a function of $1/T_p$. (B) Effect of isoalloxazine coating on E_a of MWNT oxidation. Black and red curves denote MWNT only and FMN-MWNT. (A colour version of this figure can be viewed online.)

chirality [23,30], handedness [24], and electronic type [31] of SWNTs. Especially, flavin-wrapped SWNTs shows prolonged PL stability [22] against O_2 and covalent diazonium functionalization [25], as compared to those wrapped by sodium dodecyl sulfate (SDS) which forms a O_2-permeable micelle [43]. The rigid aromatic FMN along with adjacent hydrogen bonding provides tight helical wrapping which prevents oxidation from O_2, as illustrated in Fig. 1. Therefore, the structural rigidity and self-associating ability of FMN wrapping effectively passivates MWNT surface. Recently, it was demonstrated that perylenetetracarboxylic diimide which possesses similar self-associating properties like FMN also display enhanced oxidative stability of graphene by ~38 K [44]. Altogether, the tight wrapping is a key factor to prevent basal plane oxidation of graphene surface.

4. Conclusion

In summary, the structural and thermal properties of FMN adlayer have been investigated on MWNT. The tight FMN helical assembly on MWNT with structural stability provides protective coating on MWNT and, upon high temperature annealing, releases three waters and a phosphate moiety leaving behind an *N*-penta-dienyl-isoalloxazine derivative which protects MWNT surface from oxidation. This organic residue elevates the MWNT oxidative decomposition temperature by ~90 K owing to increased activation energy against O_2. The increased oxidative stability of FMN-MWNT was confirmed by electrical measurements. Overall, these results provide insight into the interfacial factors that influence the stability of molecular adlayers on MWNT and thus provide guidance for the controlled thermal stability of organic-MWNT nanostructure.

Conflict of interest

This work was provisionally filed in the patent office.

Appendix A. Supplementary data

Supplementary data related to this article can be found at http://dx.doi.org/10.1016/j.carbon.2017.02.098.

atmosphere, the sheet resistance of the FMN-MWNT increases 6.3 times (i.e., 83 Ω/sq) while that of the bare MWNT film shows 253 times (i.e., 2300 Ω/sq). This result demonstrates the FMN wrapping on MWNT slows down electrical property decrease of MWNT by surface passivation from oxygen.

The remaining question is whether only FMN among various polymers and small molecules exhibits enhanced oxidative stability for MWNTs. In order for oxygen to bind MWNT surface, oxygen needs to penetrate surfactant wrapping. Since number of bound oxygen is expected to be a function of binding affinity of surfactant to MWNT surface and facilitates accelerated oxidation at the ends of MWNT, the binding affinity of surfactant to MWNT surface is expected to play a role to the aforementioned mobile oxygenated species. The strong binding affinity of flavin moiety among various surfactants [26] has been utilized to selectively enrich single

Fig. 10. Sheet resistances of bare MWNT (black) and FMN-MWNT films (red) before and after the 1 h 753 K annealing. Note that vertical axis has a break. (A colour version of this figure can be viewed online.)

References

[1] M.S. Dresselhaus, G. Dresselhaus, P. Avouris, Carbon Nanotubes: Synthesis, Structure, Properties and Applications, Springer, Berlin, 2001.
[2] R.H. Baughman, A.A. Zakhidov, W.A. de Heer, Carbon nanotubes-the route toward applications, Science 297 (5582) (2002) 787—792.
[3] M.F.L. De Volder, S.H. Tawfick, R.H. Baughman, A.J. Hart, Carbon nanotubes: present and future commercial applications, Science 339 (6119) (2013) 535—539.
[4] Z. Wen, Q. Wang, Q. Zhang, J. Li, In situ growth of mesoporous SnO_2 on multiwalled carbon nanotubes: a novel composite with porous-tube structure as anode for lithium batteries, Adv. Funct. Mater. 17 (15) (2007) 2772—2778.
[5] L. Dai, D.W. Chang, J.-B. Baek, W. Lu, Carbon nanomaterials for advanced energy conversion and storage, Small 8 (8) (2012) 1130—1166.
[6] N. Li, Y. Huang, F. Du, X. He, X. Lin, H. Gao, et al., Electromagnetic interference (EMI) shielding of single-walled carbon nanotube epoxy composites, Nano Lett. 6 (6) (2006) 1141—1145.
[7] L. Bokobza, Multiwall carbon nanotube elastomeric composites: a review, Polymer 48 (17) (2007) 4907—4920.
[8] A. Pantano, G. Modica, F. Cappello, Multiwalled carbon nanotube reinforced

polymer composites, Mater. Sci. Eng. A 486 (1—2) (2008) 222—227.

[9] H.G. Chae, Y.H. Choi, M.L. Minus, S. Kumar, Carbon nanotube reinforced small diameter polyacrylonitrile based carbon fiber, Compos Sci. Technol. 69 (3—4) (2009) 406—413.

[10] T. Kashiwagi, F. Du, J.F. Douglas, K.I. Winey, R.H. Harris, J.R. Shields, Nanoparticle networks reduce the flammability of polymer nanocomposites, Nat. Mater. 4 (12) (2005) 928—933.

[11] D.K. Singh, P.K. Iyer, P.K. Giri, Diameter dependence of oxidative stability in multiwalled carbon nanotubes: role of defects and effect of vacuum annealing, J. Appl. Phys. 108 (8) (2010) 084313.

[12] D.Y. Kim, C.-M. Yang, Y.S. Park, K.K. Kim, S.Y. Jeong, J.H. Han, et al., Characterization of thin multi-walled carbon nanotubes synthesized by catalytic chemical vapor deposition, Chem. Phys. Lett. 413 (1—3) (2005) 135—141.

[13] D.-Y. Kim, Y.S. Yun, S.-M. Kwon, H.-J. Jin, Preparation of aspect ratio-controlled carbon nanotubes, Mol. Cryst. Liq. Cryst. 510 (1) (2009) 79—86.

[14] J. Wang, J. Huang, R. Yan, F. Wang, W. Cheng, Q. Guo, et al., Graphene microsheets from natural microcrystalline graphite minerals: scalable synthesis and unusual energy storage, J. Mater. Chem. A 3 (6) (2015) 3144—3150.

[15] H.Y. Nan, Z.H. Ni, J. Wang, Z. Zafar, Z.X. Shi, Y.Y. Wang, The thermal stability of graphene in air investigated by raman spectroscopy, J. Raman Spectrosc. 44 (7) (2013) 1018—1021.

[16] M. Sharon, M. Sharon, H. Shinohara, A. Tiwari, Graphene: An Introduction to the Fundamentals and Industrial Applications, Wiley, 2015.

[17] A. Mahajan, A. Kingon, Á. Kukovecz, Z. Konya, P.M. Vilarinho, Studies on the thermal decomposition of multiwall carbon nanotubes under different atmospheres, Mater. Lett. 90 (2013) 165—168.

[18] C.M. White, R. Banks, I. Hamerton, J.F. Watts, Characterisation of commercially CVD grown multi-walled carbon nanotubes for paint applications, Prog. Org. Coat. 90 (2016) 44—53.

[19] L.R. Radovic, Active sites in graphene and the mechanism of CO_2 formation in carbon oxidation, J. Am. Chem. Soc. 131 (47) (2009) 17166—17175.

[20] B. Frank, A. Rinaldi, R. Blume, R. Schlögl, D.S. Su, Oxidation stability of multiwalled carbon nanotubes for catalytic applications, Chem. Mater. 22 (15) (2010) 4462—4470.

[21] V. Massey, The chemical and biological versatility of riboflavin, Biochem. Soc. Trans 28 (4) (2000) 283—296.

[22] S.-Y. Ju, W.P. Kopcha, F. Papadimitrakopoulos, Brightly fluorescent single-walled carbon nanotubes via an oxygen-excluding surfactant organization, Science 323 (5919) (2009) 1319—1323.

[23] S.-Y. Ju, J. Doll, I. Sharma, F. Papadimitrakopoulos, Selection of carbon nanotubes with specific chiralities using helical assemblies of flavin mononucleotide, Nat. Nanotechnol. 3 (6) (2008) 356—362.

[24] S.-Y. Ju, D.C. Abanulo, C.A. Badalucco, J.A. Gascón, F. Papadimitrakopoulos, Handedness enantioselection of carbon nanotubes using helical assemblies of flavin mononucleotide, J. Am. Chem. Soc. 134 (32) (2012) 13196—13199.

[25] J. Sim, H. Oh, E. Koo, S.-Y. Ju, Effect of tight flavin mononucleotide wrapping and its binding affinity on carbon nanotube covalent reactivities, Phys. Chem. Chem. Phys. 15 (44) (2013) 19169—19179.

[26] H. Oh, J. Sim, S.-Y. Ju, Binding affinities and thermodynamics of noncovalent functionalization of carbon nanotubes with surfactants, Langmuir 29 (35) (2013) 11154—11162.

[27] W. Yoon, Y. Lee, H. Jang, M. Jang, J.S. Kim, H.S. Lee, et al., Graphene nanoribbons formed by a sonochemical graphene unzipping using flavin mononucleotide as a template, Carbon 81 (2015) 629—638.

[28] M. Ayán-Varela, J.I. Paredes, L. Guardia, S. Villar-Rodil, J.M. Munuera, M. Díaz-González, et al., Achieving extremely concentrated aqueous dispersions of graphene flakes and catalytically efficient graphene-metal nanoparticle hybrids with flavin mononucleotide as a high-performance stabilizer, ACS Appl. Mater. Interfaces 7 (19) (2015) 10293—10307.

[29] Z. Gao, C. Zhi, Y. Bando, D. Golberg, T. Serizawa, Noncovalent functionalization of disentangled boron nitride nanotubes with flavin mononucleotides for strong and stable visible-light emission in aqueous solution, ACS Appl. Mater. Interfaces 3 (3) (2011) 627—632.

[30] M. Jang, S. Kim, H. Jeong, S.Y. Ju, Affinity-mediated sorting order reversal of single-walled carbon nanotubes in density gradient ultracentrifugation, Nanotechnology 27 (41) (2016), 41LT01.

[31] M. Park, S. Kim, H. Kwon, S. Hong, S. Im, S.-Y. Ju, Selective dispersion of highly pure large-diameter semiconducting carbon nanotubes by a flavin for thin film transistors, ACS Appl. Mater. Interfaces 8 (35) (2016) 23270—23280.

[32] E. Koo, S.-Y. Ju, Role of residual polymer on chemical vapor grown graphene by raman spectroscopy, Carbon 86 (2015) 318—324.

[33] A. Stolle, T. Szuppa, S.E.S. Leonhardt, B. Ondruschka, Ball milling in organic synthesis: solutions and challenges, Chem. Soc. Rev. 40 (5) (2011) 2317—2329.

[34] A.J. Lynch, C.A. Rowland, The History of Grinding: Society for Mining Metallurgy;, 2005.

[35] H.-J. Butt, B. Cappella, M. Kappl, Force measurements with the atomic force microscope: technique, interpretation and applications, Surf. Sci. Rep. 59 (1—6) (2005) 1—152.

[36] R. Sharifi, M. Samaraweera, J.A. Gascón, F. Papadimitrakopoulos, Thermodynamics of the quasi-epitaxial flavin assembly around various-chirality carbon nanotubes, J. Am. Chem. Soc. 136 (20) (2014) 7452—7463.

[37] M.S. Dresselhaus, G. Dresselhaus, R. Saito, A. Jorio, Raman spectroscopy of carbon nanotubes, Phys. Rep. 409 (2) (2005) 47—99.

[38] M.S. Dresselhaus, A. Jorio, A.G. Souza Filho, R. Saito, Defect characterization in graphene and carbon nanotubes using raman spectroscopy, Philos. T Roy. Soc. A 2010 (368) (1932) 5355—5377.

[39] J. Masłowska, M. Malicka, Thermal behaviour of riboflavin, J. Therm. Anal. 34 (1) (1988) 3—9.

[40] F. Xu, L.X. Sun, J. Zhang, Y.N. Qi, L.N. Yang, H.Y. Ru, et al., Thermal stability of carbon nanotubes, J. Therm. Anal. Calorim. 102 (2) (2010) 785—791.

[41] H.E. Kissinger, Reaction kinetics in differential thermal analysis, Anal. Chem. 29 (11) (1957) 1702—1706.

[42] C.S. Lin, R.Q. Zhang, T.A. Niehaus, T. Frauenheim, Geometric and electronic structures of carbon nanotubes adsorbed with flavin adenine Dinucleotide: a theoretical study, J. Phys. Chem. C 111 (11) (2007) 4069—4073.

[43] N.F. Hartmann, S.E. Yalcin, L. Adamska, E.H. Haroz, X. Ma, S. Tretiak, et al., Photoluminescence imaging of solitary dopant sites in covalently doped single-wall carbon nanotubes, Nanoscale 7 (48) (2015) 20521—20530.

[44] H.J. Karmel, J.J. Garramone, J.D. Emery, S. Kewalramani, M.J. Bedzyk, M.C. Hersam, Self-assembled organic monolayers on epitaxial graphene with enhanced structural and thermal stability, Chem. Commun. 50 (64) (2014) 8852—8855.

A Self-Assembled Flavin Protective Coating Enhances the Oxidative Thermal Stability of Multi-Walled Carbon Nanotubes

Somin Kim,[1] Myungsu Jang,[1] Minsuk Park,[1] No-Hyung Park,[2] and Sang-Yong Ju[1],*

[1]Department of Chemistry, Yonsei University, 50 Yonsei-ro, Seodaemun-Gu, Seoul 03722, Korea,

[2]Department of Textile Convergence of Biotechnology and Nanotechnology, Korea Institute of Industrial Technology, 1271-18 Sa 3-dong, Sangnok-gu, Ansan-Si, Gyeonggi-Do 426-910, Korea
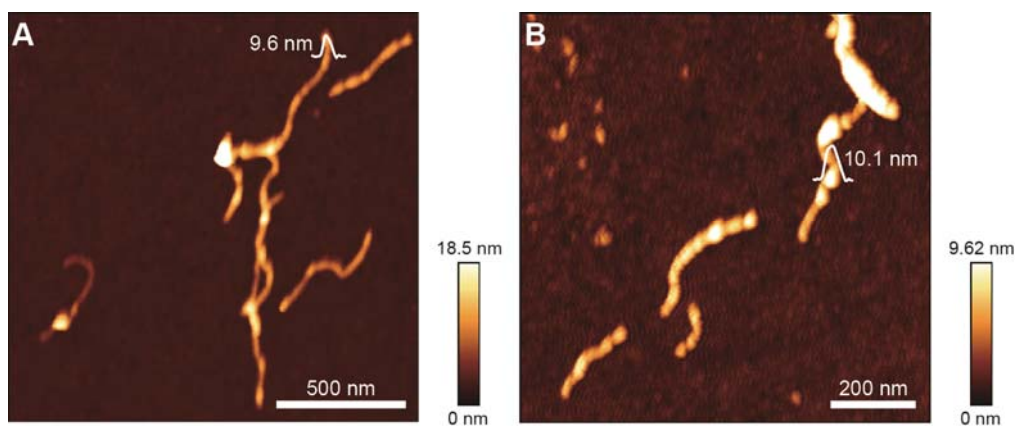
Figure S1.(A and B) The corresponding height images of FMN-MWNTs.
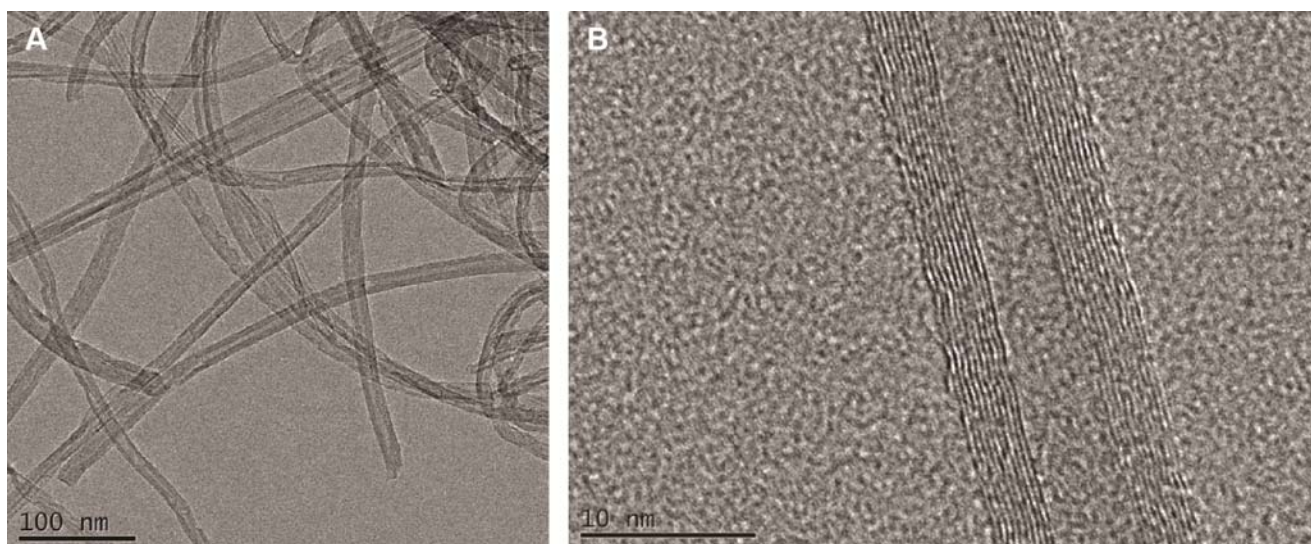
Figure S2. (A and B) TEM images of the as-received MWNT.
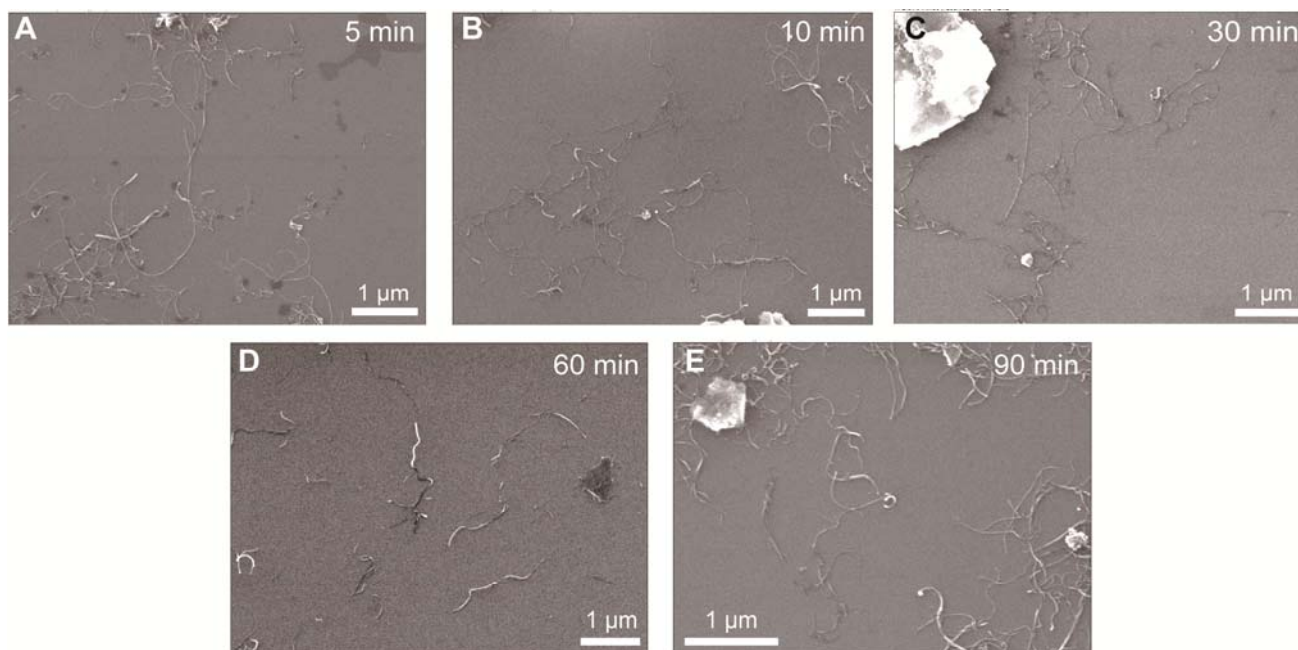
Figure S3. (A to E) SEM images of FMN-MWNTs as a function of milling time (i.e., 5, 10, 30, 60, and 90 min).
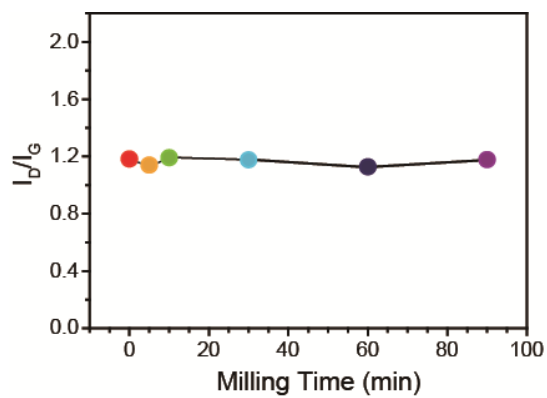
Figure S4. The corresponding I_D/I_G trend as a function of milling times from Figure 4 in the main text.
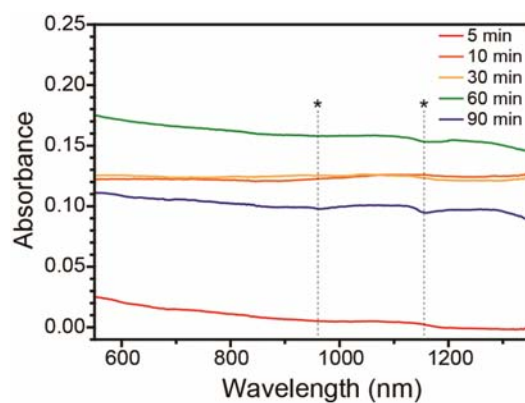
Figure S5. Absorption spectra of the supernatants of FMN-MWNTs as a function of milling time dissolved in water. Asterisks originates from water [Sim, J. *et al*., *Phys. Chem. Chem. Phys*. 2013, 15, 19169-19179].
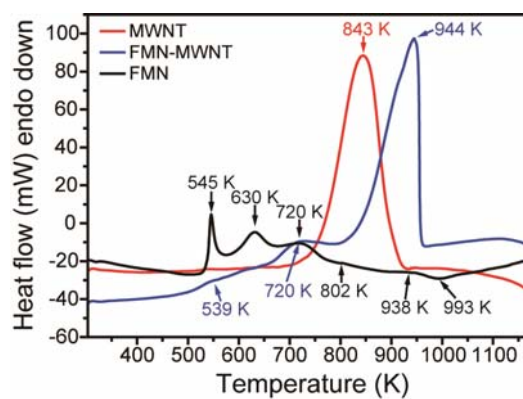
Figure S6. DSC curves of the as-received FMN, MWNT, and FMN-MWNT.
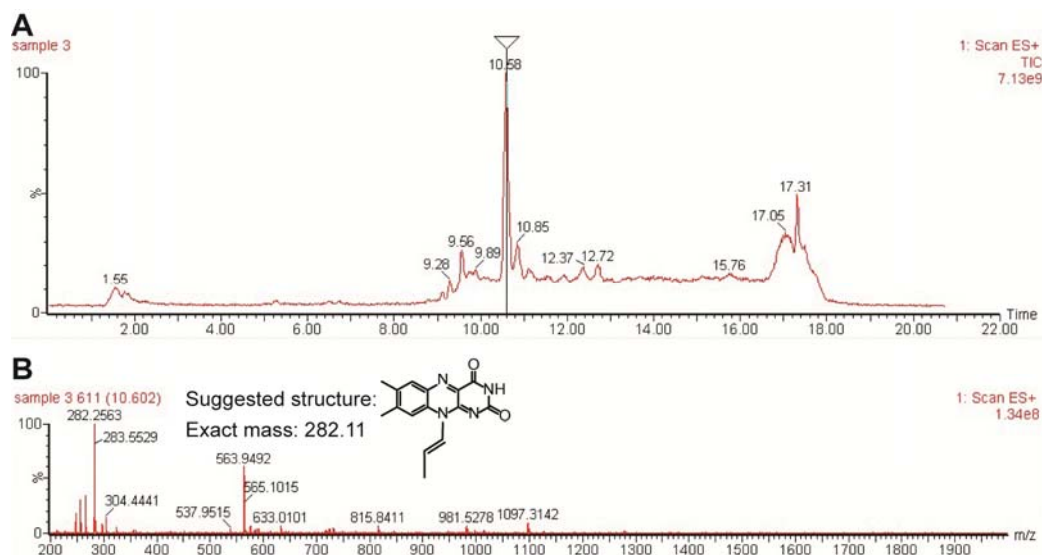
Figure S7. LC-MS spectra of the 543 K annealed FMN sample. (A) Chromatogram of the annealed sample. (B) MS spectra obtained from the maximum peak of LC at 10.6 min.
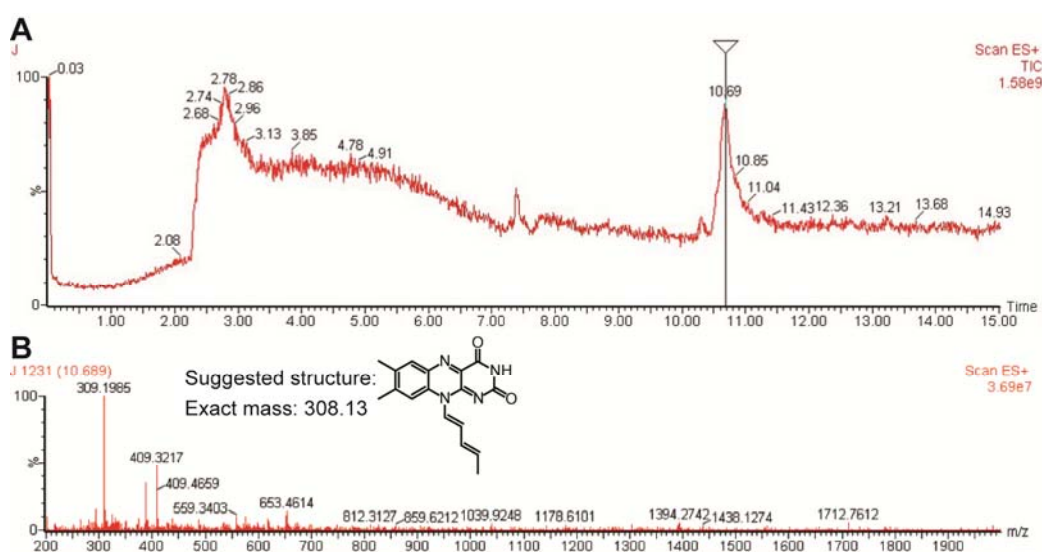
Figure S8. LC-MS spectra of the 723 K annealed FMN-MWNT sample. (A) Chromatogram of the 723 K annealed FMN-MWNT sample in DMSO, and (B) MS spectrum from the major peak from 10.69 min from the chromatogram.
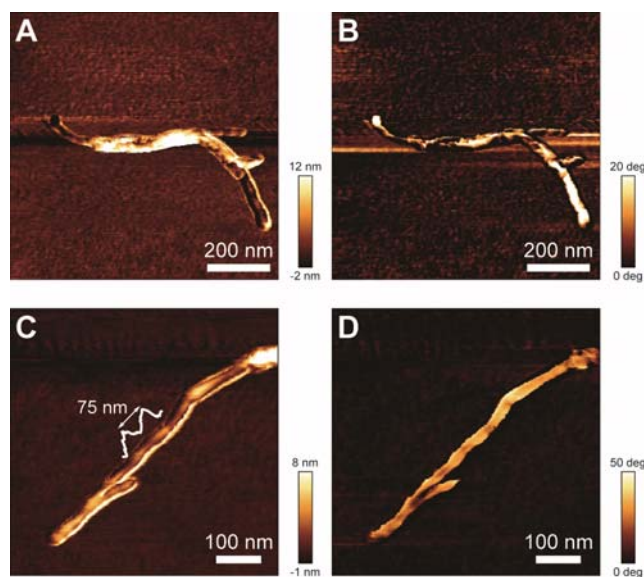
Figure S9. AFM height (A and C) and corresponding phase (B and D) images of the 723 K annealed FMN-MWNT.
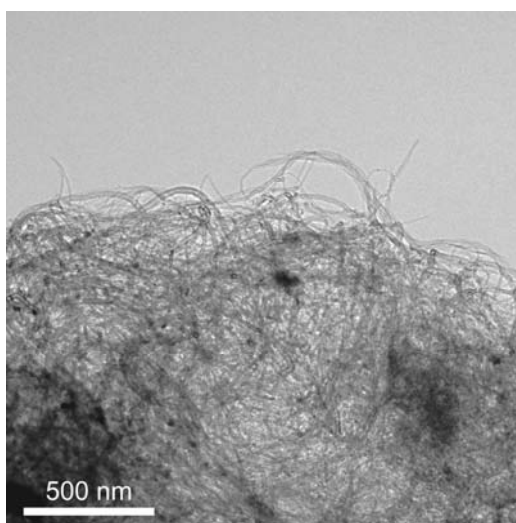
Figure S10. Additional TEM image of the 723 K annealed FMN-MWNT.
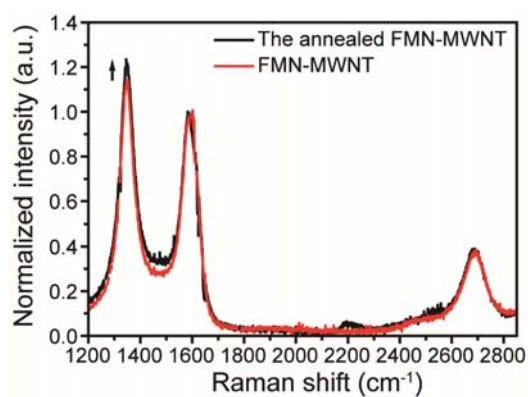
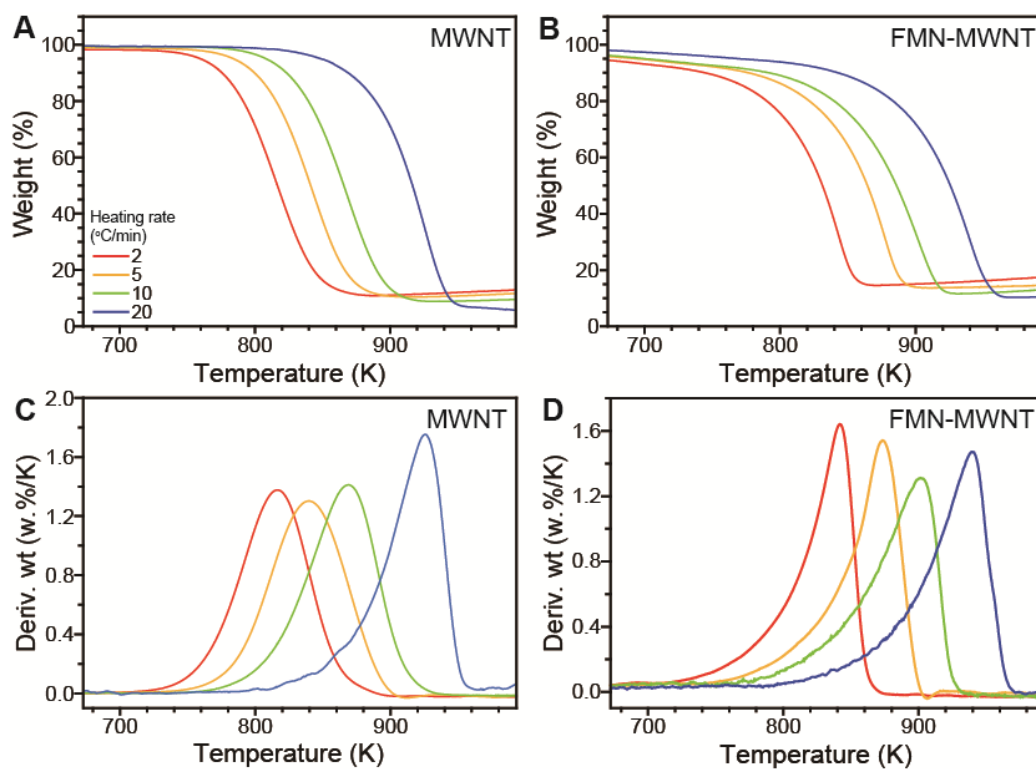**Figure S11.** Comparison of Raman spectra of the FMN-MWNT and the 723 K annealed FMN-MWNT.
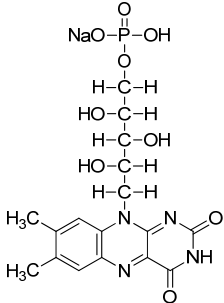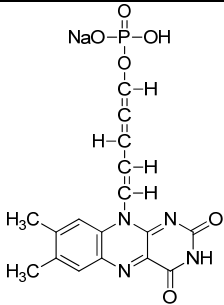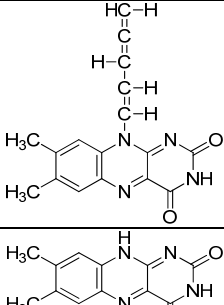

Figure S12. (A and B) TGA and (C and D) the corresponding differential curves of MWNT and the 723 K annealed FMN-MWNT obtained by using different heating rates.

Table S1. Comparison of weight % from TGA and suggested structure.

Temperature (K)	Wt % by TGA	Wt % by suggested structure	Suggested chemical structures	Wt difference (%)
303	100.00	100.00		0
543	89.61	88.70		0.91
648	67.04	64.04		3.00
713	50.08	50.64		-0.56